



Simulated and measured temperature coefficients in compensated silicon wafers and solar cells



Halvard Haug^{a,*}, Charly Berthod^b, Åsmund Skomedal^a, Jan Ove Odden^c, Erik Stensrud Marstein^a, Rune Søndena^a

^a Institute for Energy Technology, Instituttveien 18, 2007, Kjeller, Norway

^b University of Agder, Jon Lilletunsvai 9, 4879, Grimstad, Norway

^c REC Solar Norway, P.O. Box 8040 Vaagsbygd, NO-4675, Kristiansand S, Norway

ARTICLE INFO

Keywords:

Silicon
Solar cells
Device simulation
Photoluminescence
Carrier lifetime
Temperature

ABSTRACT

In this paper we perform a thorough investigation of the temperature coefficients of c-Si solar cells and wafers, based on both experimental data and device simulations. Groups of neighboring wafers were selected from different heights of four high performance multicrystalline silicon ingots cast using different dopants concentrations and Si feedstocks; Three different target resistivities of compensated silicon ingots based on Elkem Solar Silicon (ESS[®]), which are purified through a metallurgical route, and one non-compensated reference ingot. The wafers were processed into Al-BSF and PERCT type solar cells, as well as into lifetime samples subjected to selected solar cell processing steps before being etched down and re-passivated to assess the bulk lifetime of the final cells. Temperature-dependent photoluminescence imaging was used to study the spatial distribution of the carrier lifetime and the temperature coefficient of the lifetime. We observe a beneficial effect of higher doping levels on the temperature coefficients of the short circuit current J_{SC} in PERCT type cells, with the most favorable temperature coefficients are found in the ingot doped to 0.5 Ω -cm. Increasingly beneficial temperature coefficients in J_{SC} is also observed with increasing height in each ingot, which might be attributed to a combination of small variations in the dopant concentrations and to a clear increase in the temperature coefficient of the carrier lifetime with increasing ingot height. The latter point is also in agreement with the changes in the so-called gamma parameter of the open circuit voltage throughout the ingot. To build a more fundamental understanding of the experimental results the temperature dependence of the solar cells was simulated using PC1Dmod6.2. We find that the experimental temperature coefficients of the final cells can be reproduced in device simulations within 8% of and 14% for the V_{OC} and J_{SC} , respectively. The compensation level itself is of minor importance for the cell performance. Instead, the simulations indicate that the observed behavior in the temperature coefficients of the solar cells is mostly explained by differences in the net doping and carrier lifetime of the wafers.

1. Introduction

Photovoltaic energy production is growing at a considerable rate, with larger investments in solar power in 2017 than in coal, gas and nuclear power combined [1]. Reducing the energy requirement for solar grade Si production is of high importance for the continued reduction of cost and CO₂-footprint of solar energy. One proven technology in this regard is metallurgical (liquid state) purification of Si, as a more energy efficient alternative to the conventional Siemens process, where the Si is purified through highly energy demanding gas phase [2,3]. The world's largest producer of metallurgically purified silicon is REC Solar Norway (previously Elkem Solar), producing Elkem Solar

Silicon (ESS[®]) [4]. ESS[®] mainly differs from conventional polysilicon produced by the Siemens method by the presence of both boron and phosphorus dopants in the feedstock [5,6]. For p-type silicon production, the background phosphorus donor concentration is compensated for by adding additional acceptors, in the melt, hence the name compensated silicon. The compensation level, C_i , in p-type material is defined as

$$C_i = \frac{(N_A + N_D)}{(N_A - N_D)} = \frac{N_A + N_D}{p_0}, \quad (1)$$

where N_A and N_D are the ionized acceptor and donor concentrations, respectively, and p_0 is the net doping, equal to the hole concentration at

* Corresponding author.

E-mail address: halvard.haug@ife.no (H. Haug).

<https://doi.org/10.1016/j.solmat.2019.109921>

Received 16 January 2019; Received in revised form 16 April 2019; Accepted 30 April 2019

Available online 10 May 2019

0927-0248/ © 2019 Elsevier B.V. All rights reserved.

equilibrium. The typical level of phosphorus in ESS[®] is 0.60 ppmw [7]. Due to the different segregation coefficients of different dopant species, a more uniform resistivity profile throughout the height of the multicrystalline ingot can be obtained by adding Ga co-doping in addition to boron (also called tri-doping), enabling a larger degree of optimization of the resistivity towards the final solar cell performance [8–10].

Conventionally solar cells and modules are characterized in test laboratories under standard test conditions (STC), i.e. the performance is determined at 25 °C and 0.1 mW/cm² normal incidence AM1.5G irradiation (1 Sun illumination). However, the performance of cells and modules depend heavily on the temperature [11]. Under normal operation at 0.1 mW/cm² illumination the operating temperature will generally far exceed 25 °C depending on the ambient temperature [12].

Previous field studies where modules consisting of ESS[®] are compared to polysilicon reference modules with comparable performance at STC have shown that modules based on ESS[®] outperform the reference modules by 1–2% relative under high irradiation and high temperature conditions [7,13]. The authors of these studies suggested that this could be due to the compensation doping, or to differences in the base resistivity of the wafers. We have previously observed that ESS[®] wafers have a positive temperature coefficient in the carrier lifetime, which may also influence the temperature dependence of the cell performance [14]. The beneficial effect of elevated temperature and/or irradiation was also later demonstrated in more controlled laboratory experiments, but without measuring the temperature behaviour of the carrier lifetimes [15,16]. One important motivation for the present work is therefore to investigate the temperature dependence of both wafers and cells based on ESS[®] ingots with different resistivity values, as well as a non-compensated reference material, to gain a fundamental understanding of the underlying mechanisms behind these observed effects.

In order to relate the field performance to the solar cell parameters measured at STC it is useful to define a temperature coefficient TC_X , defined for any parameter X as:

$$TC_X = \frac{100\%}{X_{STC}} \cdot \frac{dX}{dT}, \quad (2)$$

where X_{STC} is the value of X at STC and dX is the change in X over the temperature interval dT . A linear dependence of the temperature characteristics of the parameter of interest can be assumed for the temperature range (25–75 °C) [17]. Increasing temperatures causes a number of physical properties of the silicon material to change, affecting the temperature sensitivity of the final solar cells. The temperature will most importantly affect the intrinsic carrier concentration, n_{i0} , as the number of thermally excited carriers strongly increase with temperature. n_{i0} is a crucial parameter in all minority carrier devices, including solar cells, and thus also plays a large role in the temperature dependence of the device. Furthermore, the band gap, E_g , narrows with increasing temperature, which in turn increases the absorption of photons, increasing the short circuit current generated in the solar cell.

Several physical properties of the Si material are affected by the compensation level of the material. A larger impact of incomplete ionization of dopants is expected [18,19], and the carrier mobilities will be reduced due to the increased number of scattering sites [20–22]. The different amounts of dopants may lead to band gap narrowing, affecting both J_{SC} and V_{OC} directly, as well as affecting the absorption of light in the material. Recent studies show, however, that the base resistivity is more important than the compensation for both the performance of the solar cell and its temperature coefficients [23,24]. Quantum efficiencies (QE) measured at different temperatures show that the main difference is in the 800–1100 nm range indicating a bulk lifetime effect. Converging QE curves towards 1200 nm indicates minimal effect of band gap narrowing on the light absorption in compensated silicon [25].

In the present work current-voltage (IV) parameters at different temperatures have been measured in order to determine the temperature coefficients of solar cells made from ingots with different feedstock blends. The same IV-parameters and their temperature behaviour have

Table 1

Description of the four center bricks from G5 ingots studied in the present work. The net doping is calculated at 50% ingot height, see Fig. 1 for more information.

Ingot name	Target resistivity	Net doping (cm ⁻³)	Dopants	Feedstock
REF	1.3 Ω-cm	1.1×10^{16}	B	Polysilicon, FBR
ESS 1.3	1.3 Ω-cm	1.3×10^{16}	B, P, Ga	ESS [®] , polysilicon
ESS 0.9	0.9 Ω-cm	1.9×10^{16}	B, P, Ga	ESS [®] , polysilicon
ESS 0.5	0.5 Ω-cm	3.8×10^{16}	B, P, Ga	ESS [®] , polysilicon

also been simulated using PC1Dmod6.2, based on measured minority carrier lifetimes in passivated wafers. Measured and simulated trends in the different temperature coefficients will be discussed.

2. Experimental details

Four different high performance multicrystalline (HPMC) silicon G5 ingots, listed in Table 1, were investigated in this work. Three ingots with target resistivities of 0.5, 0.9, and 1.3 Ω-cm were produced using a blend of 70% ESS[®] and 30% polysilicon. Gallium co-doping was used to engineer the resistivity profiles in the ingots containing compensated ESS[®] feedstock. In addition, a non-compensated ingot with target resistivity of 1.3 Ω-cm, made with a blend of Siemens polysilicon and fluidized bed reactor (FBR) silicon, was cast as a reference. The net doping, the resistivity profiles and the compensation levels throughout the ingot heights are shown in Fig. 1 based on calculations and fitting to experimental resistivity profiles published in a previous paper [8]. Note that the three ESS[®] ingots are named after their target resistivity, and that the actual resistivity is varying along the ingot height. The trends for the compensated ingots are relatively even and similar with some variations from 80% of the ingot height, while the non-compensated ingot has its resistivity decreasing along the whole height. This shows the clear advantage in resistivity engineering of compensation doping. Wafers from different heights in center bricks were then processed for measurements of their minority charge carrier lifetimes whereas wafers from neighboring positions were processed into complete solar cells.

Since the minority carrier lifetime is significantly influenced by the solar cell processing, wafers from different heights in the bricks were processed prior to carrier lifetime measurements according to the process flow shown in Fig. 2. The process is designed to produce lifetime samples with low surface recombination velocity (SRV), and where the bulk lifetime is as close as possible to that of the final solar cells: After an initial damage etch in a HNA-solution a double-sided emitter with a sheet resistance of about 80 Ω/square was diffused into the wafers in a Tempres POC₃ tube furnace. A hydrogen rich SiN_x:H anti reflective coating (ARC) is then deposited on both sides using plasma enhanced chemical vapor deposition (PECVD) in an Oxford Plasmalab 133 chamber before the wafers were subjected to a simulated contact firing process in a belt furnace. The ARC-layers were removed, and the emitters etched away in a new HNA-solution before the wafers were cleaned and surface passivated. An a-Si:H/SiN_x:H stack was deposited on both sides of the wafers using PECVD. Surface recombination velocities of less than 5 cm/s are routinely obtained using this passivation scheme [14]. Prior to lifetime measurements the wafers were light soaked with about 20 mW/cm² (LED) for 48 h at room temperature to stabilize any degradation caused by boron-oxygen defects. Minority carrier lifetimes were measured using calibrated photoluminescence (PL) imaging on a LIS-R1 setup from BTImaging [26]. Spatial lifetime maps of the wafers at different temperatures were obtained by calibrating the PL-images towards quasi steady-state photoconductance (QssPC) measurements performed at comparable temperatures [14]. Temperature dependent QssPC-measurements were performed on a WTC 120 TS lifetime tester from Sinton Instruments. The carrier lifetime images were acquired at a constant photon flux of $\phi = 1 \times 10^{17}$

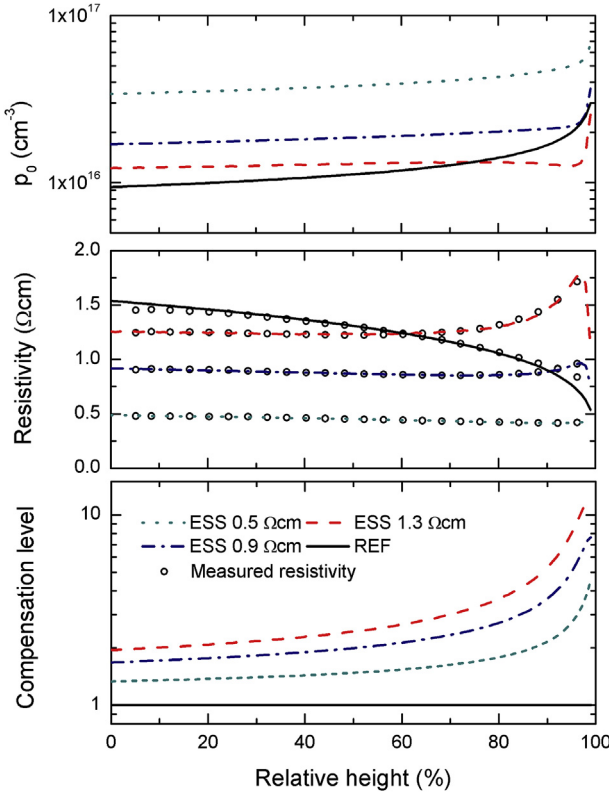


Fig. 1. The net doping as a function of height (top) is calculated using the Scheil equation, taking into account the effects of compensation doping, including incomplete ionization [8]. Corresponding resistivity profiles (middle) calculated using a compensation level-dependent mobility model implemented in PC1Dmod6.2. Experimental resistivity profiles from eddy current measurements are shown as open circles (every 5th data point is included for clarity). The estimated resistivity profiles show relatively flat profiles for large parts of the three compensated ingots, but with a marked increase towards the very top. The non-compensated ingot shows a general decrease in the resistivity with increasing height in the ingot. The compensation levels (bottom) are calculated according to Eq. (1).

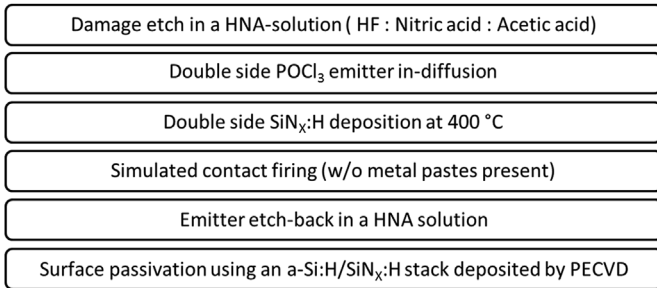


Fig. 2. The process route for wafers from different heights in the ingots intended for minority carrier lifetime measurements.

$\text{cm}^{-2}\text{s}^{-1}$, resulting in an average injection level similar to that simulated at V_{oc} conditions in the final solar cells.

Solar cells were produced from the four center bricks using wafers from different heights adjacent to the surface passivated wafers. Passivated emitter rear totally diffused (PERCT) cells with a full rear side boron diffusion were produced as described by Teppe et al. [27,28]. The solar cells were light soaked for at least 48 h to stabilize any BO-degradation before their current-voltage characteristics were measured under 1 Sun illumination using a AM1.5G solar spectrum. A triple-A sun simulator from NeonSee™ was used. Temperature coefficients were obtained by measuring the IV-characteristics from room

temperature to 70 °C with 2 °C intervals.

3. Simulation details

The temperature dependent behavior of the compensated and non-compensated silicon solar cells has been simulated using PC1Dmod 6.2, using a combination of physical models which include the effects of temperature as well as the simultaneous presence of B, P and Ga dopants [29,30]. In the recent years the device modeling tool has been updated with Fermi-Dirac statistics and several other advanced models for various material properties of crystalline silicon [31,32].

Device simulations of c-Si solar cells are normally performed at 300 K, and many commonly used constants describing material parameters are only intended for use at this temperature. We here take advantage of the fact that many of the recently implemented models in PC1Dmod6.2 include both the temperature and compensation doping dependence of various quantities. The most important of these is the exponential increase in the intrinsic carrier density n_{i0} with T and its negative effect on the V_{oc} , which accounts for approximately 80–90% of the temperature dependence of a c-Si solar cell [17]. To understand this temperature dependence of the V_{oc} , it is useful to consider an ideal, 1-diode model of the solar cell:

$$J = J_0 \exp\left(\frac{qV}{k_B T} - 1\right) - J_{ph}. \quad (3)$$

Here, q is the electron charge, k_B is the Boltzmann constant, T is the cell temperature, J_{ph} is the photogenerated current and J_0 is the saturation current density, given for an ideal diode as

$$J_0 = q \left(\frac{D_N}{L_N N_A} + \frac{D_p}{L_p N_D} \right) n_{i0}^2, \quad (4)$$

where D_N and $L_N = \sqrt{D_N \times \tau_N}$ is the electron diffusivity and diffusion length, respectively, with τ_N being the electron minority carrier lifetime (and similarly for holes). The main temperature dependence of J_0 is determined by the term n_{i0}^2 , which is given by:

$$n_{i0}^2 = n_0 p_0 = N_C N_V \exp\left(\frac{-E_g(T)}{k_B T}\right) \quad (5)$$

where N_C and N_V represent the effective densities of states in the conduction band and valence band, respectively [33]. N_C and N_V each vary with temperature approximately as $T^{3/2}$, resulting in an ideal temperature dependence of $J_0 = CT^3 \exp\left(\frac{qV}{k_B T}\right)$, where C is a constant independent of T . Additional temperature dependency (e.g. in D or τ), can be accounted for analytically by replacing the exponent 3 with a more general parameter γ , so that

$$J_0 = CT^\gamma \exp\left(\frac{qV}{k_B T}\right). \quad (6)$$

γ can take values from 1.2 in the radiative limit up to 5 for a solar cell dominated by space charge region recombination [34]. By inserting this expression into (Eq. (3)), solving at open circuit conditions ($J = 0$ and $V = V_{oc}$), setting $E_g = E_{g0} + (dE_g/dT) \times T$ and taking the derivative we arrive at the following expression for $TC_{V_{oc}}$, first introduced in Ref. [17]:

$$TC_{V_{oc}} = \frac{1}{V_{oc}} \frac{dV_{oc}}{dT} = -\frac{1}{V_{oc}} \frac{1}{T} \left(\frac{E_{g0}}{q} - V_{oc} + \gamma \frac{kT}{q} \right) \quad (7)$$

where E_{g0} is the extrapolated bandgap at zero kelvin.

One large advantage of using numerical device simulations is of course that all the assumptions used to arrive at these analytical expressions are not needed, but they are still highly useful for understanding the relative importance of the different physical models. Many simulation tools define $n_{i0}(T)$ based on theoretical models for $N_C(T)$, $N_V(T)$ and $E_g(T)$. However, because n_{i0} is vital for determining solar cell performance and is generally known to a better precision than N_C

and N_V , PC1D5 and now PC1Dmod6.2 have chosen to define this parameter directly as a material property, together with E_g and the ratio N_C/N_V , to always keep consistency with Eq. (5) [32]. In PC1Dmod6.2 $n_i(T)$ is defined by the temperature dependent model of Sproul and Green [35], scaled to match the commonly accepted value of Altermatt et al. [36] of $n_i = 9.65 \times 10^9 \text{ cm}^{-3}$ at 300 K. For the simulations in this paper the ratio N_C/N_V has been held constant at its default value and Green's model is used for the intrinsic band gap energy [37]. Note that the breakdown of n_{i0} into N_C , N_V and E_g is mostly relevant in highly doped regions, where Fermi-Dirac statistics are noticeable. For a full description of the band structure parameters in PC1Dmod, see Refs. [32,38].

In addition to n_{i0} , the temperature will also affect the cell performance through secondary effects. In PC1Dmod6.2 these include Schenk's model for band gap narrowing, the models of Altermatt et al. [18,19] and Forster et al. [39] for incomplete ionization of P, B and Ga dopants, respectively, and the model from Schindler et al. for mobility in compensated material [20]. Note that the Richter model [40] for intrinsic recombination used in this work does not take temperature into account, and changes in the emitter and bulk recombination related to temperature dependent Auger recombination in the emitter is therefore not included. We however expect this to be of small importance for the currently investigated cell architectures, a result that was also found by Steinkemper et al. [33] for the case of similar Al-BSF solar cells.

In addition to the models included in the downloadable version of PC1Dmod, a few extra modifications were needed to correctly account for the temperature dependency in the compensated Si cells. Most importantly, the model for $E_{g0}(T)$ used in PC1Dmod only influences the electrical band gap, and the increased absorption coefficient caused by lowering of the optical band gap at higher temperatures has therefore been included by modifying the external file used to define the absorption coefficient, based on the data from Nguyen et al. [41]. A small change was also made to the existing model for incomplete ionization of dopants to account for the simultaneous presence of P, B and Ga dopants in the material.

Other cell parameters were taken from experimental input (including emitter dopant profiles measured by E-CV, J_{0e} values measured by QssPC on emitter test samples, spectrally dependent reflectance, contact shading from the metal grid, etc). The bulk doping and compensation was set based on calculated P, B and Ga concentrations at each ingot height, as described in Ref. [8] and in Fig. 2. The rear side surface recombination velocity (SRV) in the PC1Dmod model was used as a free parameter to match the experimental cell results. The SRV is often empirically observed to increase with the substrate doping, so the SRV was parameterized as $SRV = a + b \times (p_0/10^{16} \text{ cm}^{-3})$ to avoid too many free parameters and at the same time obtain a good agreement with the experimental data.

Finally, the temperature dependent lifetime images were used as input to the 1D model by performing a harmonic average over the image and setting this as the bulk lifetime of the cell. The harmonic average of the lifetime image is defined as

$$\tau_{\text{harmonic}} = \left[\frac{1}{N} \sum_{i=1}^N \left(\frac{1}{\tau_i} \right) \right]^{-1} \quad (8)$$

and is generally considered to be a better representation of the impact of the carrier lifetime on the cell performance than the standard average, as it puts more weight on low lifetime areas [42]. A list of key parameters for the PC1Dmod cell model is given in Table 2.

4. Results and discussion

4.1. Lifetimes throughout ingot heights

The harmonic average carrier lifetimes from PL-images of the

Table 2

Selected cell parameters for the PC1Dmod 6.2 simulations presented in this work.

Parameter	Value
Wafer thickness	190 μm
Lumped series resistance	0.73 Ωcm^2
Front side shading	5.5%
Effective rear SRV (cm/s)	$320 \times p_0/10^{16}\text{cm}^{-3} + 30$ (Al-BSF) $150 \times p_0/10^{16}\text{cm}^{-3} + 20$ (PERCT)
Dopant concentration	Ingot height dependent (from Fig. 1)
Minority carrier lifetime	Ingot height dependent (from Fig. 3)
Front n + diffusion	Measured profile, $\rho_{\text{sheet}} = 90 \Omega \text{ cm}$
Front side surface charge	10^{12} cm^{-2}
Front SRV parameter S_{0n}	3×10^{15} (fit to $J_{0e} = 100 \text{ fA/cm}^2$)
Front reflectance	Experimental curve, texture + ARC
Absorption coefficient	T-dependent, external file (Ref [41])

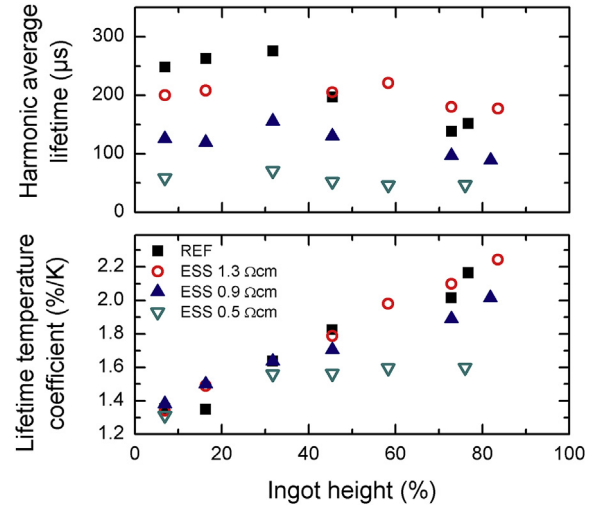


Fig. 3. Harmonic average lifetimes (top) are obtained using QssPC calibrated PL-imaging of the whole wafers. The corresponding relative temperature coefficient of the lifetime value (bottom) is based on measurements at 25 °C and 75 °C. All PL images were acquired at a constant generation rate of $5.3 \times 10^{18} \text{ cm}^{-3}\text{s}^{-1}$.

wafers are shown as a function of relative height in the ingots in Fig. 3. Wafers from the highly doped ESS 0.5 Ωcm ingot has the lowest average lifetimes with values of $\langle \tau \rangle_{\text{harmonic}}$ between 50 and 65 μs for all heights. With a reduction in the doping levels in the ESS 0.9 Ωcm and ESS 1.3 Ωcm , the average $\langle \tau \rangle_{\text{harmonic}}$ the ingots are $\sim 150 \mu\text{s}$ and $\sim 275 \mu\text{s}$, respectively. The highest harmonic lifetimes are found in the non-compensated reference ingot with an average value of $\sim 300 \mu\text{s}$. Two general trends in $\langle \tau \rangle_{\text{harmonic}}$ can be seen for most of the ingots; (1) a slight increase with height in the bottom part of the ingots, and (2) a decrease in the top part of the ingots, particularly for the reference ingot. The first trend may be explained with the small grainsize and corresponding large area fraction of grain boundaries expected near the bottom of hpmc-Si ingots [43]. With height the grain sizes tend to grow, reducing the overall lifetime limiting effect of grain boundaries (GB's). Towards the top of ingots there is a tendency of emerging growth of dislocation clusters, partly responsible for causing the reduced lifetime observed here [43,44]. In addition, there is a considerable increase of dopants, and probably also other fast diffusing impurities, potentially contributing to the lowered lifetimes measured towards the top of the ingots, illustrated by the resistivity changes and compensation levels shown in Fig. 1. The effects of increasing grain sizes and growth of dislocation clusters with increasing height in the ingots can be seen in the PL-images shown in Fig. 4, which shows lifetime maps for the four ingots at 45% and 82% height, respectively. A clear tendency towards

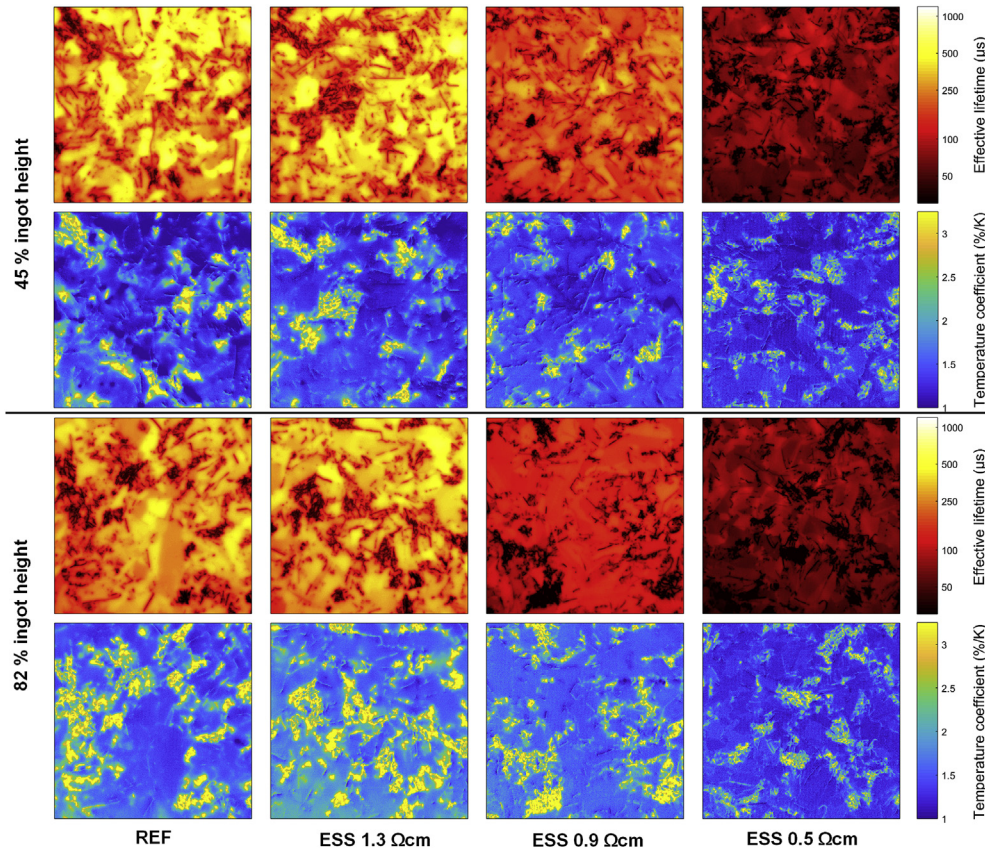


Fig. 4. Spatial distribution of carrier lifetime (top) and corresponding temperature coefficients (bottom) for wafers from the middle (45% height) and top (~80% height) position of all the ingots. Note the logarithmic scaling on the lifetime maps to allow comparison of all images on the same scale. All PL images were acquired at a constant generation rate of $5.3 \times 10^{18} \text{ cm}^{-3} \text{ s}^{-1}$.

larger, high lifetime grains and at the same time larger areas of dislocation clusters is seen at the top, particularly for the reference ingot. Fig. 3 also shows that the relative temperature coefficient of the harmonic lifetime TC_τ seem to increase with height in all the ingots. The TC_τ values are quite comparable in the bottom parts of the ingots. Ingot ESS 0.5 $\Omega\text{-cm}$ and to a lesser degree ingot ESS 0.9 $\Omega\text{-cm}$ present a smaller increase of their temperature coefficient of the lifetime than the two other ingots.

Spatial distributions of lifetimes and corresponding temperature coefficients for wafers from the middle and top position of all the ingots are shown in Fig. 4. The four ingots generally show similar behavior in the TC_τ maps, with generally positive values over the entire images. One general observation we make is that high lifetime areas largely coincide with low TC_τ areas, whereas low lifetime areas such as grain boundaries and dislocation rich areas, have higher temperature coefficients. This is in agreement with previous results by Eberle et al. [45], shown in both wafers and cells. The overall increase in TC_τ from the middle to the top of the ingot shown in Fig. 3 is also clearly visible in the maps, with an exception for ESS 0.5 $\Omega\text{-cm}$. This is mainly caused by a larger area fraction of high TC_τ (and low lifetime) areas in the top wafers.

4.2. Measured and simulated cell performance and temperature coefficients, ingot comparison

In the following we have focused the discussion on the V_{oc} and J_{sc} values of the cells, as the temperature dependence of the fill factor depend on various properties related to contacting which are not simulated in PC1Dmod. All IV-parameters for both Al-BSF and PERCT solar cells, averaged over each ingot, are shown in Table 3.

The V_{oc} and J_{sc} values for Al-BSF and PERCT cells averaged over the height of each ingot are shown in Fig. 5 together with the corresponding temperature coefficients. Both experimental and simulated

Table 3

The four main IV-parameters for the four bricks. Values for Al-BSF and PERCT cells are averaged over the height of the brick.

	Al-BSF				PERCT			
	η	V_{oc}	J_{sc}	FF	η	V_{oc}	J_{sc}	FF
	(%)	(V)	(mA/cm ²)	(%)	(%)	(V)	(mA/cm ²)	(%)
REF	17.6	0.640	34.7	79.3	19.0	0.650	36.8	79.2
ESS 1.3 $\Omega\text{-cm}$	17.6	0.641	34.7	79.3	18.9	0.649	36.7	79.2
ESS 0.9 $\Omega\text{-cm}$	17.6	0.643	34.4	79.4	18.9	0.652	36.5	79.4
ESS 0.5 $\Omega\text{-cm}$	17.2	0.644	33.5	79.6	18.7	0.654	36.0	79.6

values are included in the figure. The simulated values for both the IV-parameters as well as the corresponding temperature coefficients are all within 14% of the measured values for the PERCT cells and within 8% for the Al-BSF cells. Note that the error bars indicate the standard deviation in the spread in the data along the height of the ingots. The measured J_{sc} values are quite comparable for the REF and ESS 1.3 $\Omega\text{-cm}$ ingots, and there is a decreasing trend in J_{sc} with decreasing resistivity for the three ESS[®] ingots, which is also recreated in the simulations. This is also seen in the $TC_{J_{sc}}$, showing an increasing trend with decreasing resistivity for both cell types.

This is well reproduced by the simulations. In addition, the non-compensated reference brick has a clearly lower $TC_{J_{sc}}$ than all the ESS[®] bricks for PERCT cells. These cells are more sensitive to changes in the base diffusion length than the Al-BSF cells due to the improved surface passivation. In addition to the generation rate, the J_{sc} is also determined by the collection efficiency, which improves with higher diffusion length. The mobility, and thus the diffusion length, decreases with temperature in this temperature range, but according to Schindler's mobility model [20] the relative change in mobility with increasing temperature is smaller in compensated material. This could be one

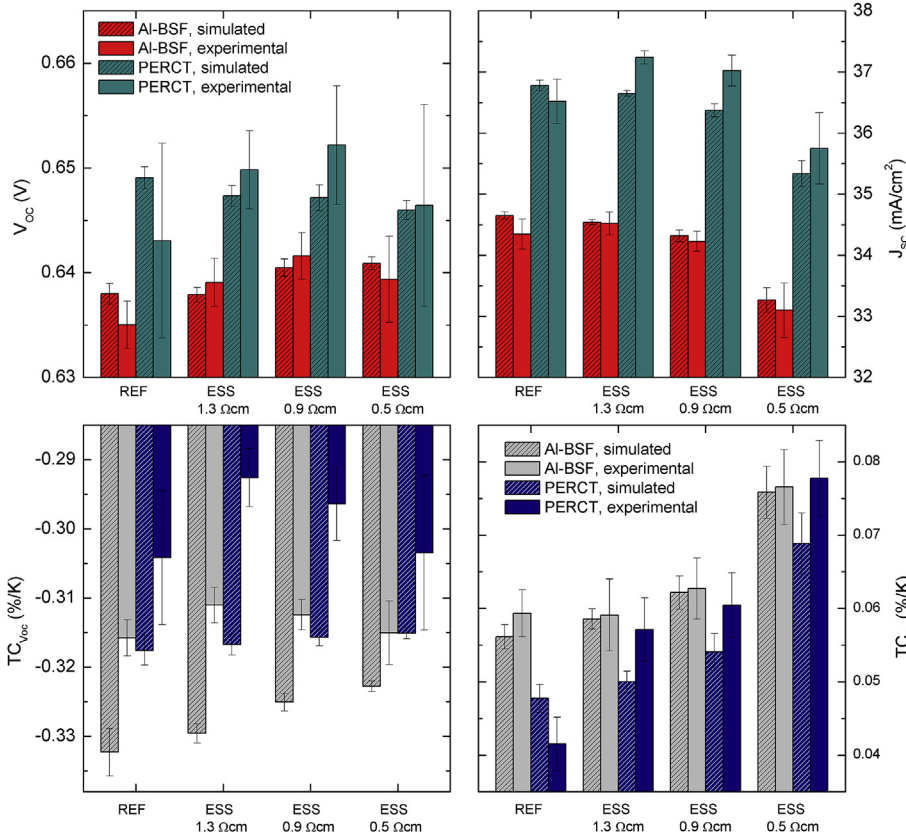


Fig. 5. Average values (top) and temperature coefficients (bottom) for the V_{OC} (left) and the J_{SC} (right) for 4 different multicrystalline ingots cast using different feedstock. Measured and simulated values for both Al-BSF and PERCT cells are shown. Error bars indicate the standard deviation in the spread of the data over the height of each ingot.

possible explanation for the observed improvements in $TC_{J_{SC}}$ for the cells based on compensated ESS[®] material.

For Al-BSF cells the REF ingot is quite comparable to the ESS 1.3 Ωcm ingot. In comparison an increasingly negative $TC_{V_{OC}}$ with decreasing resistivity for the three compensated ingots is predicted using PC1Dmod6.2 for both Al-BSF and PERCT cells, but the measured values are relatively constant for the PERCT cells, and an opposite trend is measured for the Al-BSF cells.

4.3. Measured and simulated temperature coefficients as a function of ingot height

Experimental and simulated values for the temperature coefficients for the V_{OC} and the J_{SC} are shown in Fig. 6 as a function of ingot height. The $TC_{V_{OC}}$ increases (becomes less negative) with increasing ingot height until 60–80% depending on the cell architecture. The following decrease of $TC_{V_{OC}}$ at the top of the ingot is a combination of a decreasing V_{OC} (not shown here) and an increase in the γ values (see discussion below). The simulated $TC_{V_{OC}}$ values are relatively constant with height and are generally ~ 0.02 $\%/K$ ($\sim 6\%$ relative difference) more negative than the experimental data. However, we still consider this to be of acceptable agreement, showing that the overall temperature dependence in the various physical models in the simulations give physically meaningful results. The temperature coefficients of the J_{SC} show that the ESS 0.5 Ωcm cells have the most favorable $TC_{J_{SC}}$ at $\sim 0.075\%/K$, whereas the non-compensated reference improve the least with increasing temperature. This fact is also found in the simulations, which generally show excellent agreement for the Al-BSF cells and reasonably good agreement for the PERCT cells. We observe a general trend with increasing $TC_{J_{SC}}$ with height for all the four ingots, which is also found in the simulations. Sensitivity analysis of the simulation model (not shown) indicates that this effect is caused by a combination of the dopant concentration and the improved temperature coefficient in the carrier lifetime with height, making it useful to separately consider the

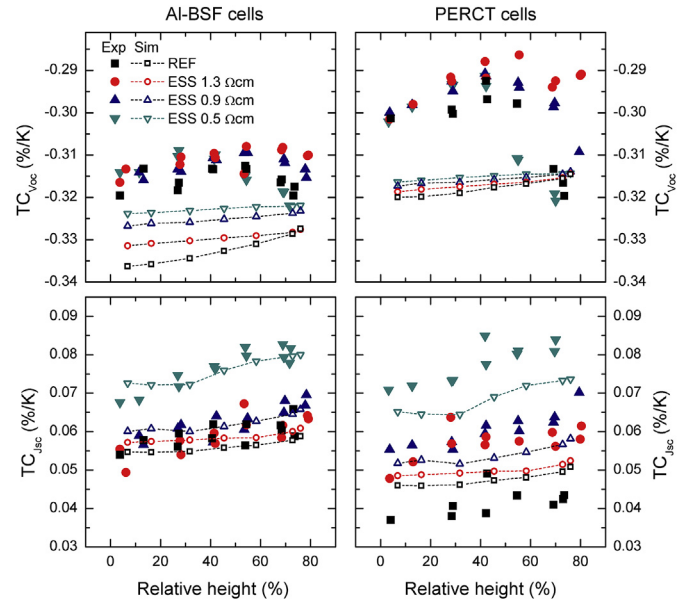


Fig. 6. Experimental and simulated values for $TC_{V_{OC}}$ (top) and $TC_{J_{SC}}$ (bottom) as a function of relative ingot height for Al-BSF (left) and PERCT type (right) solar cells. Simulated values are obtained using the PC1Dmod6.2 simulation described in section 3, with input from the harmonic average lifetimes shown in Fig. 3.

γ parameter as introduced in Eq. (6). In Fig. 7 the γ parameter is calculated from the experimental data and presented as a function of relative height for each ingot. We observe that Al-BSF cells have larger values for γ than the PERCT cells, which might be caused by the fact that these cells are more limited by surface recombination, as discussed in Ref. [34].

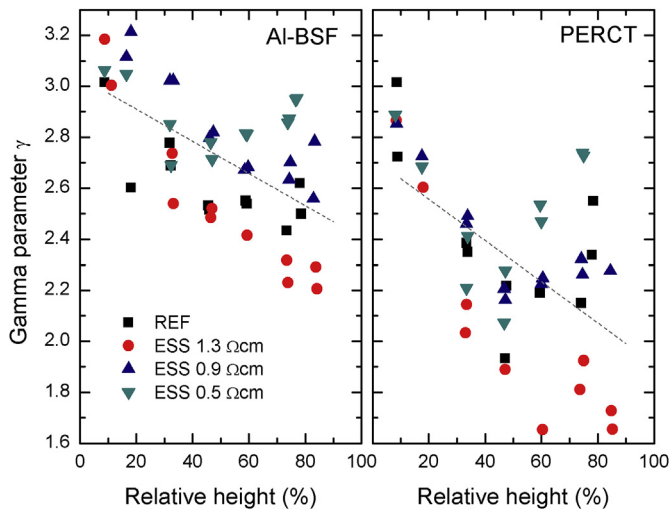


Fig. 7. γ -values extracted from Eq. (4) for both Al-BSF and PERCT solar cells. The dashed lines indicate a linear regression through all the data points for each cell type. The decreasing trend with ingot height is in good agreement with the lifetime temperature coefficients measured on wafer level, as shown in Fig. 3.

The values of TC_{Voc} are partly determined by V_{oc} . Ingot ESS 1.3 Ω -cm sees its γ decreasing over the whole ingot height for both cell types. On the other hand, the three other ingots have γ values decreasing until approximately 50% of relative height, before the values flatten out or start to increase. This is even more pronounced for the PERCT cells. Deviations from the ideal diode case ($\gamma = 3$) is determined by other temperature dependencies in the prefactor part of J_0 , which precisely include the recombination lifetime. A higher TC_τ therefore is expected to decrease the negative temperature dependence of J_0 by a general decrease in γ , and this is indeed also what we observe in the cell data: As seen in Fig. 3, ingot ESS 1.3 Ω -cm has the largest increase of TC_τ , and also the largest corresponding decrease of γ along the ingot height. Ingot ESS 0.5 Ω -cm shows the opposite with the smallest increase of TC_τ along the ingot height and has the largest values of γ on top of the ingot. Moreover, γ values are relatively similar for all ingots at the bottom of the ingot, as seen also for the TC_τ . The observed temperature dependence in the recombination of the wafers and the cells are thus in good agreement. The average injection level in the temperature dependent lifetime images is close to that of the V_{oc} conditions in the final cells, allowing for a more direct comparison.

Note that the positive temperature coefficient for the carrier lifetime and corresponding improvement in the temperature coefficients of V_{oc} and J_{sc} is also observed for the REF ingot in this case and does thus not seem to be related to the compensation level itself. To investigate this point, the simulations were repeated with and without compensation doping enabled, always keeping the same net doping density. This showed a negligible effect on the temperature coefficients for the compensation levels considered in this work, and only had a noticeable effect for very high compensation levels. We therefore conclude that the previously observed beneficial temperature coefficients in modules produced with ESS[®] wafers discussed in the introduction is not related to the fact that the material is compensated, but to resistivity differences and to the high positive TC_τ of the wafers, which is mostly determined by the casting process. The temperature coefficients of the solar cells investigated in this work are also in the upper (less negative) range of typically reported values, e.g. as summarized by Steinkemper et al. [33].

5. Summary

The minority carrier lifetimes in wafers as well as the IV-parameters of cells from different heights in four HPMC-Si ingots have been

studied. Three of the ingots are based on compensated silicon containing boron, gallium and phosphorus, whereas the non-compensated reference is only doped with boron. The dopant profiles and corresponding resistivities of the tri-doped ingots show a relatively stable value throughout the height of the ingots, whereas the resistivity varies from 0.5 to 1.5 Ω -cm for the non-compensated ingot. Thus, tri-doping allow for advanced engineering of the resistivity profiles without sacrificing the yield. On the other hand, the compensation level is considerably increased by this method.

The harmonic average carrier lifetime was observed to increase with increasing resistivity. Since HPMC-Si ingots were studied there is also a considerable variation of the silicon quality between the ingots due to crystal defects. Despite the variations in the harmonic average lifetime in the different ingots, the temperature coefficients of the lifetime are comparable. We observe a clear trend of increasing TC_τ with height along the ingots. The ESS 0.5 Ω -cm ingot and to a smaller degree also the ESS 0.9 Ω -cm ingot demonstrates smaller increase of the TC_τ . By analysis of PL images, this increase was found to mainly arise from a higher area fraction of low lifetime areas, which generally show higher temperature coefficients than high lifetime areas. From the IV measurements, we find increasing TC_{Jsc} values with increasing height in all the four ingots, which might be related to improved collection efficiency due to the higher positive temperature coefficient in the carrier lifetime. TC_{Jsc} also increases with decreasing resistivity for the three compensated ingots, and the lowest values are here found in the reference ingot, most likely due to the smaller relative decrease in mobility with temperature for compensated material and higher doping. The PC1Dmod6.2 simulations show good agreement for TC_{Jsc} as a function of height for all ingots, whereas the trends in TC_{Voc} are not reproduced in the simulations. The simulated TC_{Voc} values are however still in reasonable agreement with the experiment, within 8% and 15% for the Al-BSF cells and the PERCT cells, respectively, thus demonstrating that the implemented models give physically meaningful results. Furthermore, we find a clear relation between TC_τ measured on the wafers and the γ parameter measured on the corresponding cells, indicating that the observed differences in TC_{Voc} are partly caused by the temperature coefficient of the bulk lifetime. Sensitivity analysis based on PC1Dmod6.2 simulations showed that the observed differences in the cell temperature coefficients is probably not caused by the compensation doping itself, but rather by differences in the net doping and in the temperature coefficient of the bulk lifetime. We therefore believe that this is also the most probable explanation for the previously observed improvement of the temperature coefficient in field studies of modules based on ESS[®] material.

Acknowledgements

Funding for this work was provided through the EnergiX programme of the Norwegian Research Council, project number 256271 - Performance and Reliability IN Compensated Elkem Solar Silicon.

References

- [1] A. McCrone, U. Moslener, F. D'Estais, C. Grüning, Global Trends in Renewable Energy Investments, (2018) 2018.
- [2] J.O. Odden, G. Halvorsen, H. Rong, R. Glöckner, Comparison of the energy consumption in different production processes for solar grade silicon, Silicon for the Chemical and Solar Industry IX, Oslo, Norway, 2008.
- [3] A.-K. Soiland, M.G. Dolmen, J. Heide, U. Thisted, G. Halvorsen, G. Ausland, K. Friestad, P. Preis, K. Peter, O. Graf, T. Bartel, R. Tronstad, First results from a simplified Elkem Solar route—input to tolerance limits, Sol. Energy Mater. Sol. Cells 130 (2014) 661–667.
- [4] M.J. de Wild-Scholten, R. Glöckner, Environmental footprint of Elkem solar Silicon[®], Silicon for the Chemical and Solar Industry XI, Bergen, Norway, 2012.
- [5] A.-K. Soiland, J.O. Odden, B. Sandberg, K. Friestad, J. Håkedal, E. Enebak, S. Braathen, Solar silicon from a metallurgical route by Elkem Solar: a viable alternative to virgin polysilicon, CSSC-6, Aix-les-Bains, France, 2012.
- [6] M. Tayyib, J.O. Odden, E.H. Dahl, P. Baggehus, T.O. Sætre, Elkem silicon vs polysilicon: a quantitative impurity element analyses, 28th EUPVSEC, Paris, France,

- 2013.
- [7] J.O. Odden, T.C. Lommasson, M. Tayyib, J. Vedde, T. Buseth, K. Friestad, H. Date, R. Tronstad, Results on performance and ageing of solar modules based on Elkem Solar Silicon (ESSTM) from installations at various locations, *Sol. Energy Mater. Sol. Cells* 130 (2014) 673–678.
 - [8] R. Søndenå, H. Haug, A. Song, C.-C. Hsueh, J.O. Odden, Resistivity profiles in multicrystalline silicon ingots featuring Gallium co-doping, *AIP Conf. Proc.* 1999 (2018) 130016.
 - [9] A. Cuevas, M. Forster, F. Rougieux, D. Macdonald, Compensation engineering for silicon solar cells, *Energy Procedia* 15 (2012) 67–77.
 - [10] M. Forster, E. Fourmond, R. Einhaus, H. Lauvray, J. Kraiem, M. Lemiti, Ga co-doping in Cz-grown silicon ingots to overcome limitations of B and P compensated silicon feedstock for PV applications, *Phys. Status Solidi C* 8 (2011) 678–681.
 - [11] O. Dupré, R. Vaillon, M.A. Green, A full thermal model for photovoltaic devices, *Sol. Energy* 140 (2016) 73–82.
 - [12] D. Faiman, Assessing the outdoor operating temperature of photovoltaic modules, *Prog. Photovoltaics Res. Appl.* 16 (2008) 307–315.
 - [13] M. Tayyib, J.O. Odden, N. Ramchander, M.B. Prakash, T.S. Surendra, R. Muneeshwar, A.V. Sarma, M. Ramanjaneyulu, T.O. Sætre, A materials perspective on one full years performance of multicrystalline Si PV modules in a grid-connected system, 28th EUPVSEC, Paris, France, 2013.
 - [14] H. Haug, R. Søndenå, M.S. Wiig, E.S. Marstein, Temperature dependent photoluminescence imaging calibrated by photoconductance measurements, *Energy Procedia* 124 (2017) 47–52.
 - [15] F. Tanay, S. Dubois, N. Enjalbert, J. Veirman, Low temperature-coefficient for solar cells processed from solar-grade silicon purified by metallurgical route, *Prog. Photovoltaics* 19 (2011) 966–972.
 - [16] M. Tayyib, J.O. Odden, T.O. Sætre, Irradiance dependent temperature coefficients for MC solar cells from Elkem solar grade silicon in comparison with reference polysilicon, *Energy Procedia* 55 (2014) 602–607.
 - [17] M.A. Green, General temperature dependence of solar cell performance and implications for device modelling, *Prog. Photovoltaics Res. Appl.* 11 (2003) 333–340.
 - [18] P.P. Altermatt, A. Schenk, G. Heiser, A simulation model for the density of states and for incomplete ionization in crystalline silicon. I. Establishing the model in Si:P, *J. Appl. Phys.* 100 (2006) 113714.
 - [19] P.P. Altermatt, A. Schenk, B. Schmihusen, G. Heiser, A simulation model for the density of states and for incomplete ionization in crystalline silicon. II. Investigation of Si:As and Si:B and usage in device simulation, *J. Appl. Phys.* 100 (2006) 113715.
 - [20] F. Schindler, M. Forster, J. Broisch, J. Schön, J. Giesecke, S. Rein, W. Warta, M.C. Schubert, Towards a unified low-field model for carrier mobilities in crystalline silicon, *Sol. Energy Mater. Sol. Cells* 131 (2014) 92–99.
 - [21] D. Macdonald, A. Cuevas, Recombination in compensated crystalline silicon for solar cells, *J. Appl. Phys.* 109 (2011) 043704.
 - [22] S. Dubois, N. Enjalbert, J.P. Garandet, Effects of the compensation level on the carrier lifetime of crystalline silicon, *Appl. Phys. Lett.* 93 (2008) 032114.
 - [23] C. Berthod, R. Strandberg, J.O. Odden, T.O. Sætre, Reduced temperature sensitivity of multicrystalline silicon solar cells with low ingot resistivity, *IEEE 43rd PVSC*, Portland, Oregon, 2016.
 - [24] C. Berthod, S.T. Søndergaard, J.O. Odden, Experimental investigation of the optimal ingot resistivity for both the cell performances and the temperature coefficients for different cell architectures, WCPEC-7, Waikoloa, Hawaii, 2018.
 - [25] R. Søndenå, C. Berthod, J.O. Odden, A.-K. Søiland, M.S. Wiig, E.S. Marstein, Temperature dependent quantum efficiencies in multicrystalline silicon solar cells, *Energy Procedia* 77 (2015) 639–645.
 - [26] T. Trupke, B. Mitchell, J.W. Weber, W. McMillan, R.A. Bardos, R. Kroeze, Photoluminescence imaging for photovoltaic applications, *Energy Procedia* 15 (2012) 135–146.
 - [27] A. Teppe, C. Gong, O. Voigt, I. Melnyk, S. Keller, M. Klenk, F. Binaie, A. Samadi, J. Dong, K. Zhao, J. Liu, S. Wang, S. Zhou, P. Fath, Bifacial multicrystalline solar cells with efficiencies above 18% prepared in an industrial production environment, 31st EUPVSEC, Hamburg, Germany, 2015.
 - [28] A. Teppe, C. Gong, K. Zhao, J. Liu, S. Wang, J. Dong, S. Zhou, S. Keller, M. Klenk, I. Melnyk, P. Fath, Progress in the industrial evaluation of the mc-Si PERCT technology based on boron diffusion, *Energy Procedia* 77 (2015) 208–214.
 - [29] D.A. Clugston, P.A. Basore, PC1D version 5: 32-bit solar cell modeling on personal computers, 26th IEEE PVSC, Anaheim, California, 1997.
 - [30] H. Haug, J. Greulich, PC1Dmod 6.2 – improved simulation of c-Si devices with updates on device physics and user interface, *Energy Procedia* 92 (2016) 60–68.
 - [31] H. Haug, B.R. Olaisen, Ø. Nordseth, E.S. Marstein, A graphical user interface for multivariable analysis of silicon solar cells using scripted PC1D simulations, *Energy Procedia* 38 (2013) 72–79.
 - [32] H. Haug, A. Kimmerle, J. Greulich, A. Wolf, E.S. Marstein, Implementation of Fermi-Dirac statistics and advanced models in PC1D for precise simulations of silicon solar cells, *Sol. Energy Mater. Sol. Cells* 131 (2014) 30–36.
 - [33] H. Steinkemper, I. Geisemeyer, M.C. Schubert, W. Warta, S.W. Glunz, Temperature-dependent modeling of silicon solar cells— e_g , n_i , recombination, and V_{OC} , *IEEE J. Photovoltaics* 7 (2017) 450–457.
 - [34] O. Dupré, R. Vaillon, M.A. Green, Physics of the temperature coefficients of solar cells, *Sol. Energy Mater. Sol. Cells* 140 (2015) 92–100.
 - [35] A.B. Sproul, M.A. Green, Intrinsic carrier concentration and minority-carrier mobility of silicon from 77 to 300 K, *J. Appl. Phys.* 73 (1993) 1214–1225.
 - [36] P.P. Altermatt, A. Schenk, F. Geelhaar, G. Heiser, Reassessment of the intrinsic carrier density in crystalline silicon in view of band-gap narrowing, *J. Appl. Phys.* 93 (2003) 1598–1604.
 - [37] M.A. Green, Intrinsic concentration, effective densities of states, and effective mass in silicon, *J. Appl. Phys.* 67 (1990) 2944.
 - [38] H. Haug, J. Greulich, A. Kimmerle, E.S. Marstein, PC1Dmod 6.1 – state-of-the-art models in a well-known interface for improved simulation of Si solar cells, *Sol. Energy Mater. Sol. Cells* 142 (2015) 47–53.
 - [39] M. Forster, A. Cuevas, E. Fourmond, F.E. Rougieux, M. Lemiti, Impact of incomplete ionization of dopants on the electrical properties of compensated p-type silicon, *J. Appl. Phys.* 111 (2012) 043701.
 - [40] A. Richter, S.W. Glunz, F. Werner, J. Schmidt, A. Cuevas, Improved quantitative description of Auger recombination in crystalline silicon, *Phys. Rev. B* 86 (2012) 165202.
 - [41] H.T. Nguyen, F.E. Rougieux, B. Mitchell, D. Macdonald, Temperature dependence of the band-band absorption coefficient in crystalline silicon from photoluminescence, *J. Appl. Phys.* 115 (2014) 43710.
 - [42] H. Haug, M.S. Wiig, R. Søndenå, J. Wong, Simulating the effect of lifetime non-uniformity on solar cell performance using cmd-PC1D 6 and Griddler 2, *Energy Procedia* 92 (2016) 69–74.
 - [43] G. Stokkan, Y. Hu, Ø. Mjøs, M. Juel, Study of evolution of dislocation clusters in high performance multicrystalline silicon, *Sol. Energy Mater. Sol. Cells* 130 (2014) 679–685.
 - [44] K.E. Ekstrøm, G. Stokkan, A. Autruffe, R. Søndenå, H. Dalaker, L. Arnberg, M. Di Sabatino, Microstructure of multicrystalline silicon seeded by polysilicon chips and fluidized bed reactor granules, *J. Cryst. Growth* 441 (2016) 95–100.
 - [45] R. Eberle, S.T. Haag, I. Geisemeyer, M. Padilla, M.C. Schubert, Temperature coefficient imaging for silicon solar cells, *IEEE J. Photovoltaics* 8 (2018) 930–936.